ACS APPLIED MATERIALS & INTERFACES

Research Article

www.acsami.org

Amorphous GeO_x-Coated Reduced Graphene Oxide Balls with Sandwich Structure for Long-Life Lithium-Ion Batteries

Seung Ho Choi,[†] Kyeong Youl Jung,[‡] and Yun Chan Kang*,[†]

[†]Department of Materials Science and Engineering, Korea University, Anam-Dong, Seongbuk-Gu, Seoul 136-713, Republic of Korea

[‡]Department of Chemical Engineering, Kongju National University, 275 Budae-dong, Cheonan, Chungnam 330-717, Republic of Korea

Supporting Information

ABSTRACT: Amorphous GeO_x-coated reduced graphene oxide (rGO) balls with sandwich structure are prepared via a spray-pyrolysis process using polystyrene (PS) nanobeads as sacrificial templates. This sandwich structure is formed by uniformly coating the exterior and interior of few-layer rGO with amorphous GeO_x layers. X-ray photoelectron spectroscopy analysis reveals a Ge:O stoichiometry ratio of 1:1.7. The amorphous GeO_x-coated rGO balls with sandwich structure have low charge-transfer resistance and fast Li^+-ion diffusion rate. For example, at a current density of 2 A g^{-1}, the GeO_x-coated rGO balls with sandwich and filled structures and the commercial GeO_2 powders exhibit initial charge capacities of 795, 651, and 634 mA h g^{-1}, respectively; the corresponding 700th-cycle charge capacities are 758, 579, and 361 mA h g^{-1}. In addition, at a current density of 5 A g^{-1}, the rGO balls with sandwich structure have a 1600th-cycle reversible charge capacity of 629 mA h g^{-1} and a corresponding capacity retention of 90.7%, as measured from the maximum reversible capacity at the 100th cycle.

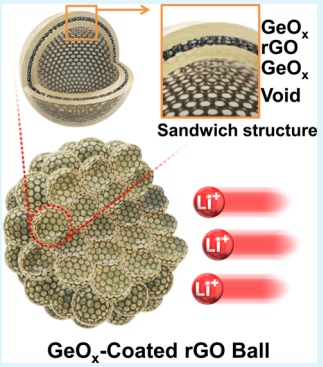

KEYWORDS: *germanium oxide, graphene composite, anode material, lithium-ion battery, spray pyrolysis*

1. INTRODUCTION

Owing to their high theoretical capacities, group IVA elements (Si, Ge, and Sn) have attracted attention as promising anode materials for lithium (Li)-ion batteries.[1−20] Of these elements, Ge with properties such as high reversible capacity (~1600 mA h g^{-1}), fast Li-ion ion diffusivity, and high electrical conductivity is the most well-suited for use as anode materials.[14−20] Ge can store 4.4 mol of Li ion/mol of Ge via Li−Ge alloying. Therefore, Ge undergoes a large volume change upon Li-ion insertion/extraction, which leads to pulverization and loss of the electrical contact in, and hence capacity fading of, the electrode.[14−20] Recently, Ge-based compounds, such as GeO_2, GeO_x, GeS, and GeSe, were found to exhibit significantly better cycling stability than pure Ge.[21−32] This improved cycling and rate performance stems from the Ge metal nanocrystals, dispersed in the Li_2O, Li_2S, or Li_2Se matrix, which were formed by the electrochemical conversion reaction of Ge compounds in the first discharge process (Li-ion insertion process).[21−32] Considering the two-dimensional (2D) nature of reduced graphene oxide (rGO), an ideal second-phase material should be 2D as well, so that a surface-to-surface contact can be formed.[33] The 2D metal oxide/rGO composite with high structural stability during repeated Li insertion and desertion processes had an ideal structure as anode materials for Li-ion batteries. To the best of our knowledge, 2D GeO_x/rGO composite with sandwich structure has not been reported in the previous literature.

In previous studies, carbonaceous materials, such as graphene, amorphous carbon, and carbon nanotubes, were successfully applied as buffer layers in order to accommodate the large volume change of the active materials.[34−41] Owing to their high electronic conductivity, carbonaceous materials combined with active materials facilitate high Li-ion mobility, which results in excellent high rate performance.[34−41] Therefore, composites of nanostructured germanium oxide (GeO_2) and carbonaceous materials have also been developed. For example, Jin et al. synthesized vertically aligned graphene@amorphous GeO_x nanoflakes, which exhibited a stable capacity of 1008 mA h g^{-1} and an excellent rate performance.[21] Similarly, Lv et al. successfully synthesized a self-assembled GeO_x/rGO composite via a facile one-step reduction approach; the well-dispersed rGO sheets, nanosized particles, and amorphous phase significantly enhanced the electron transfer and lithiation/delithiation kinetics in the composite.[22] There, the rGO sheets acted as a critical buffer layer against capacity degradation in the fabricated electrodes.

In this study, and for the first time ever, amorphous GeO_x-coated rGO composite powders with sandwich structure were prepared via a spray-pyrolysis process, which uses polystyrene (PS) nanobeads as sacrificial templates. Porous rGO balls retain the outstanding intrinsic properties of rGO sheets, such as large surface area, novel physical properties, and excellent electrical conductivity.[42−47] These balls facilitate fast electron transfer into the electron collector and can also serve as a void space for

Received: April 1, 2015
Accepted: June 5, 2015
Published: June 5, 2015

DOI: 10.1021/acsami.5b02846
ACS Appl. Mater. Interfaces 2015, 7, 13952−13959

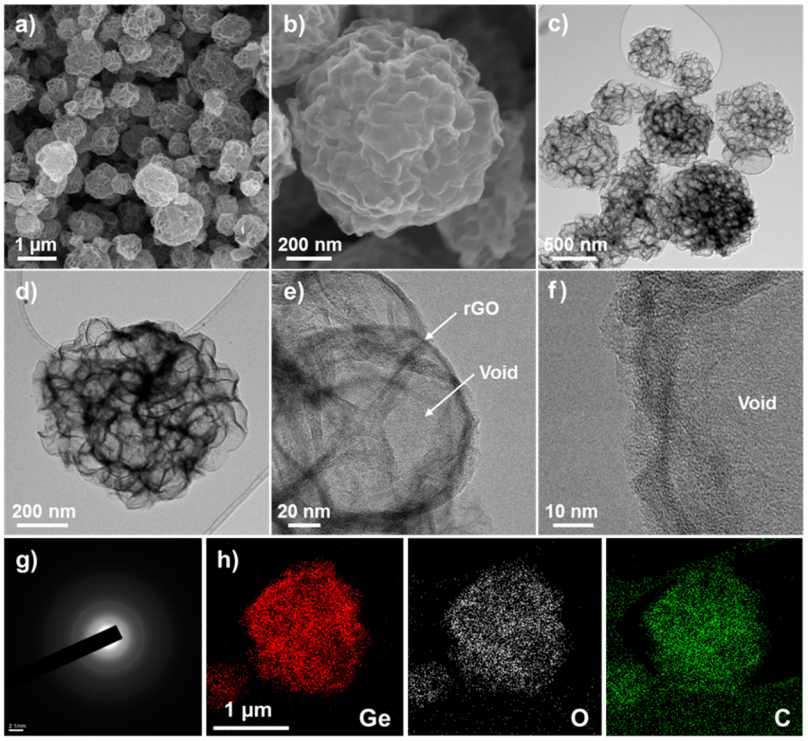

Figure 1. Morphologies, SAED pattern, and elemental mapping images of the amorphous GeO_x-coated rGO composite powders with sandwich structure: (a and b) FE-SEM, (c–e) TEM, and (f) HR-TEM images; (g) SAED pattern; (h) elemental mapping images of the Ge, O, and C components.

volume expansion of the electroactive materials during Li insertion and extraction. The spray-pyrolysis process also produced large amounts of dense, uniform coatings of amorphous GeO_x in the rGO ball.

2. EXPERIMENTAL DETAILS

Synthesis Method. Graphene oxide (GO) was synthesized using a modified Hummer's method.[47] The as-obtained GO was redispersed in distilled water and exfoliated by ultrasonication in order to generate GO sheets. A portion (500 mL) of the exfoliated GO solution (1 mg mL^{-1}) was added to 1.5 g of germanium oxide (GeO_2; Samchun Chem.) and 20 mL of ammonia solution (NH_4OH; Samchun Chem.). Then, 3.0 g of 100 nm polystyrene (PS) nanobeads was added to the solution of GO sheets and GeO_2. PS nanobeads were synthesized by an emulsion-free polymerization. Styrene (30.0 mL), sodium 4-styrnenesulfonic acid (0.25 g), and sodium carbonate (0.15 g) were dissolved in water (300 mL), and the solution was stirred at 70 °C for 1 h. Thereafter, potassium persulfate (0.15 g) was added, and the solution was vigorously stirred by a fluid mixer (300 rpm) at 70 °C for 18 h under a nitrogen atmosphere. PS nanobeads in the spray solution bonded to GO through hydrophobic interactions and helped dispersion of the GO sheets in the spray solution.[48,49] GeO_x/rGO balls were subsequently prepared by ultrasonic spray pyrolysis at 700 °C using a 1200 mm (length) × 50 mm (diameter) quartz reactor, with an argon-gas flow rate (carrier gas) of 5 L min^{-1}. The schematic diagram of the spray-pyrolysis process was shown in Figure S1 in the Supporting Information (SI). In addition, the aqueous spray solution without PS nanobeads was used to prepare crumpled GeO_2/rGO composite microspheres.

Characterization. The crystal structures of the powders were determined via X-ray diffraction (XRD; X'pert PRO MPD), using Cu Kα radiation (λ = 1.5418 Å). Moreover, the morphological features were investigated using field-emission scanning electron microscopy (FE-SEM; Hitachi S-4800) and high-resolution transmission electron microscopy (HR-TEM; JEM-2100F) at an accelerating voltage of 200 kV. The specific surface areas of the microspheres were calculated from a Brunauer–Emmett–Teller (BET) analysis of the nitrogen adsorption measurements (TriStar 3000). These microspheres were also examined using X-ray photoelectron spectroscopy (XPS; ESCALAB-210) with Al Kα radiation (1486.6 eV). Furthermore, thermal gravimetric analysis (TGA; SDT Q600) was performed in air at a heating rate of 20 °C min^{-1} in order to determine the amount of graphene in the powders.

Electrochemical Measurements. The capacities and cycling properties of the GeO_x-coated porous graphene balls were determined using a 2032-type coin cell format. The electrode was prepared from a mixture containing 70 wt % active material, 20 wt % Super P, and 10 wt % poly(acrylic acid) binder. Li metal and microporous polypropylene film were used as the counter electrode and separator, respectively. The electrolyte used was a solution of 1 M $LiPF_6$ in a 1:1 volume mixture of ethylene carbonate/dimethyl carbonate to which 5 wt % fluoroethylene carbonate was added. In addition, the charge/discharge characteristics of the samples were determined by cycling in a potential range of 0.001–3.0 V at fixed current densities. Cyclic voltammetry (CV) was performed at a scan rate of 0.1 mV s^{-1}. The dimensions of the negative electrode were 1 cm × 1 cm, and the mass loading of active materials was approximately 1.2 mg cm^{-2}. Furthermore, electrochemical impedance spectroscopy (EIS) was performed at frequencies ranging from 100 kHz to 0.01 Hz.

3. RESULTS AND DISCUSSION

Figure 1 shows the morphologies of the GeO_x/rGO composite powders that were prepared directly by spray pyrolysis from the spray solution containing PS nanobeads. The SEM images (Figure 1a,b) reveal the embossed structure of the spherical composite powders. The drying of droplet-containing PS nanobeads formed the composite powder with the embossed structure as an intermediate product. The powders formed from the decomposition of $Ge_5O_{11}^{-}$ and the thermal reduction of GO into rGO; the nanovoids in the powders were generated by decomposition of the PS nanobeads.[48] TEM images (Figure

DOI: 10.1021/acsami.5b02846
ACS Appl. Mater. Interfaces 2015, 7, 13952–13959

Scheme 1. Schematic Diagram for the Formation Mechanism of the Amorphous GeO_x-Coated rGO Composite Powder with Sandwich Structure

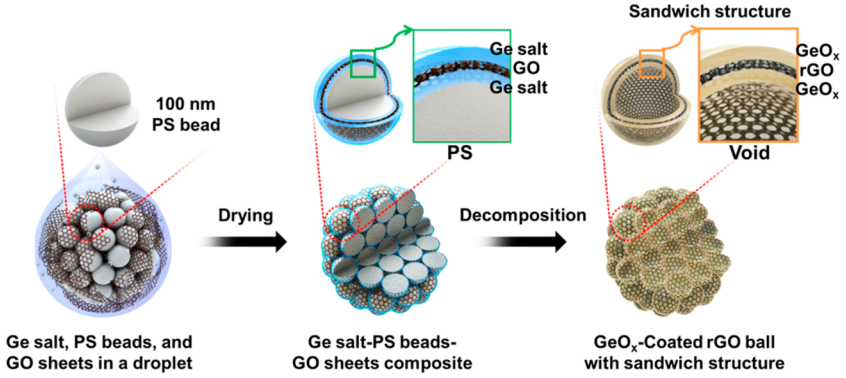

1c–e) reveal that these nanovoids are uniformly dispersed in the powder. Although the GeO_x crystals were not observed in the HR-TEM images (Figure 1e,f), the selected-area electron diffraction (SAED) pattern (Figure 1g) shows the amorphous-like structure of the composite powder. In addition, the elemental mapping images (Figure 1h) show that the Ge and C components are uniformly distributed in the powder. The amorphous GeO_x layers, which were not observed from the HR-TEM images, are also uniformly distributed over the embossed rGO ball; a schematic of the embossed GeO_x/rGO composite powder is shown in Scheme 1. The powder has a sandwich structure and consists of a thin wall, which has a thickness of several nanometers. The exterior and interior of few-layer rGO were uniformly coated with amorphous GeO_x layers in order to form the sandwich structure. This scheme shows that the multiple coating layers of the Ge salt–GO–Ge salt, which cover the PS nanobeads, were formed by the drying of the droplet. Moreover, the multilayered sandwich-structured GeO_x@rGO@GeO_x results from decomposition of the Ge salt into amorphous GeO_x and the thermal reduction of GO into rGO. Figure 2 shows the morphologies of the GeO_x/rGO composite powders, which were prepared directly by spray pyrolysis from the spray solution without PS nanobeads. These composite powders had crumpled and filled structures (Figure 2a–c); the HR-TEM image (Figure 2d) shows the rGO layers, as indicated by the arrow. GeO_x crystals were, however, not observed in this image. The crumpled GeO_x/rGO composite powders with filled structure are also composed of amorphous GeO_x layers, which are uniformly dispersed therein.

Figure 3 shows the results of XRD, XPS, TGA, and BET of the GeO_x-coated rGO composites with sandwich and filled structures. The XRD patterns (Figure 3a) of the composites prepared by using the spray solutions with and without PS nanobeads are consistent with those of amorphous materials. The thin amorphous GeO_x layer resulted from the uniform distribution of GeO_x on the rGO layers. Peaks corresponding to crystalline GeO_x are absent from the XRD pattern.[21−23] However, as Figure S2 in the SI shows, the XRD pattern of the commercial GeO_2 powders exhibits peaks that are associated with the GeO_2 crystal. The broad peaks at 25° in the XRD pattern of the sandwich-structured GeO_x-coated rGO balls (Figure 3a) are attributed to the diffraction of rGO nanosheets and short-range-ordered Ge–O structures in amorphous GeO_x.[22] XPS analysis was performed in order to identify the chemical state of Ge in the two types of composites. The Ge 3d peak in the XPS profile could be separated into five

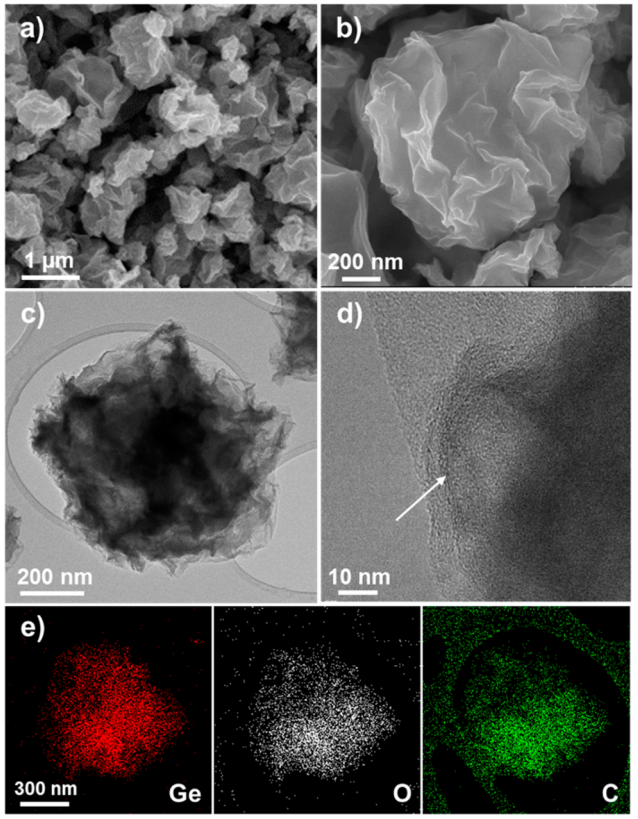

Figure 2. Morphologies and elemental mapping images of the amorphous GeO_x-coated rGO ball composite powders with filled structure: (a and b) FE-SEM, (c) TEM, and (d) HR-TEM images; (e) elemental mapping images of the Ge, O, and C components.

components, namely, Ge^0, Ge^+, Ge^{2+}, Ge^{3+}, and Ge^{4+}, which correspond to peaks at 29.3, 30.1, 31.1, 32.0, and 32.6 eV, respectively.[50] In addition, the main peak, at 32.5 eV, of the Ge 3d spectrum (Figure 3b) was fitted to three separate peaks centered at 31.1, 32.0, and 32.6 eV corresponding to Ge^{2+}, Ge^{3+}, and Ge^{4+}, respectively. These Ge 3d components accounted for 23% (Ge^{2+}), 31% (Ge^{3+}), and 32% (Ge^{4+}) of the total composite.[50] Furthermore, the absence of a peak at 29.3 eV indicates that there was no elementary Ge metal in the sandwich-structured GeO_x-coated rGO balls. In fact, the XPS Ge 3d result revealed a Ge:O stoichiometry ratio of 1:1.7. The Ge 3d spectrum of the GeO_x-coated rGO balls with filled structure that were prepared from the spray solution without

DOI: 10.1021/acsami.5b02846
ACS Appl. Mater. Interfaces 2015, 7, 13952–13959

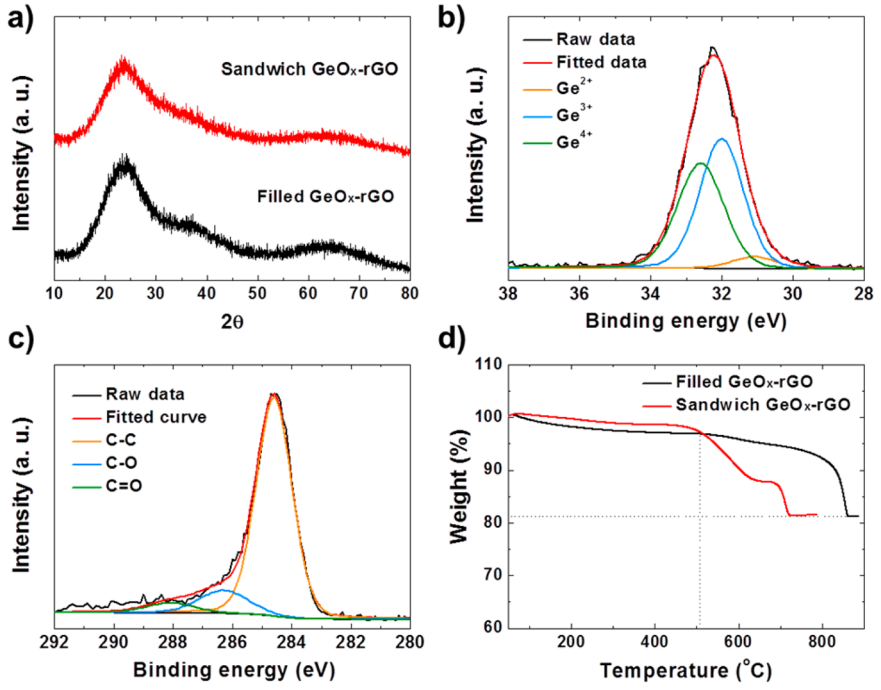

Figure 3. Properties of the amorphous GeO_x-coated rGO composite powders with sandwich and filled structures: (a) XRD patterns; (b) XPS Ge 3d spectrum of the composite with sandwich structure; (c) XPS C 1s spectrum of the composite with filled structure; (d) TG curves of both samples.

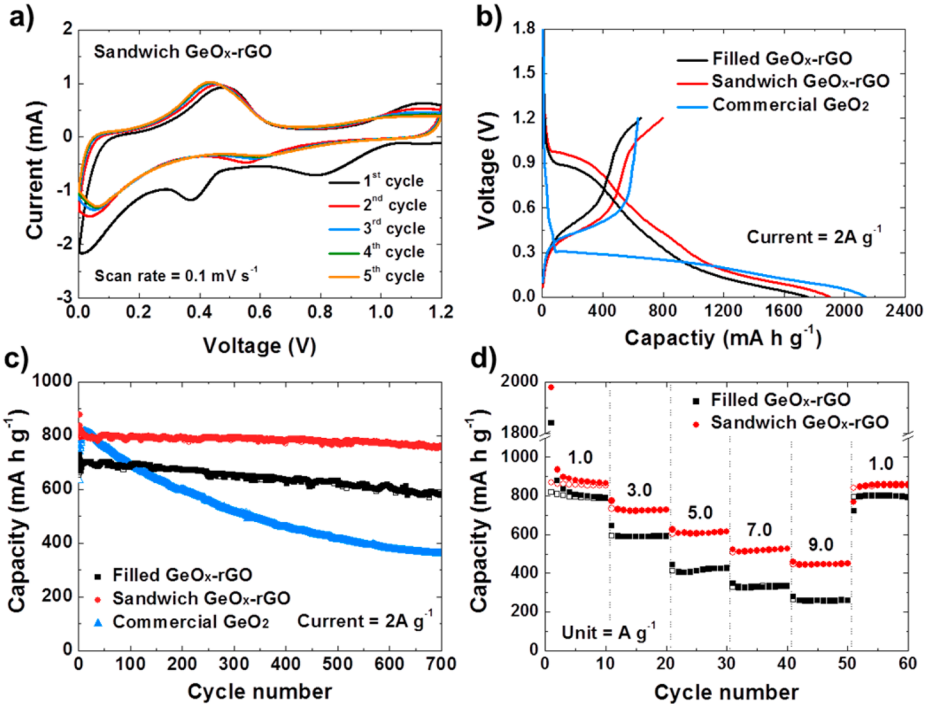

Figure 4. Li-ion storage properties of the amorphous GeO_x-coated rGO composite powders with sandwich and filled structures and commercial GeO_2 powders: (a) CV curves of the composite with sandwich structure; (b) initial charge/discharge curves at a current density of 2 A g^{-1}; (c) cycling performances at a current density of 2 A g^{-1}; (d) rate performances of the amorphous GeO_x-coated rGO composite.

PS nanobeads also has a main peak at 32.5 eV, as shown in Figure S3 in the SI. This peak was fitted to two separate peaks centered at 32.0 and 32.6 eV, which correspond to Ge^{3+} and Ge^{4+}, respectively. These low oxidation states resulted from the enhanced reducing atmosphere around the composite powders. The main peak, at 285.0 eV, in the C 1s spectrum of the GeO_x-coated rGO balls with sandwich structure (Figure 3c) was fitted to three separate peaks centered at 284.6, 286.6, and 288.1 eV. These peaks correspond to sp^2-bonded carbon (C−C), epoxy and alkoxy groups (C−O), and carbonyl and carboxylic (C═O) groups, respectively.[51,52] The sharp peak at ∼284.6 eV corresponds to the thermal reduction of GO into rGO for both the sandwich-structured and densely structured GeO_x-coated rGO balls. The Raman spectrum of the amorphous GeO_x-

DOI: 10.1021/acsami.5b02846
ACS Appl. Mater. Interfaces 2015, 7, 13952−13959

coated rGO composite powders was investigated to confirm the reduction of GO into rGO. The Raman spectrum shown in Figure S4 in the SI consisted of two peaks, one around 1360 cm^{-1} called the D peak (disordered or amorphous) and another around 1598 cm^{-1} called the G peak (graphite).[53,54] The high peak intensity of the D band suggested an increase of the defects on the GO nanosheets by thermal reduction.[54] Moreover, the thermogravimetric (TG) curves (Figure 3d) of the rGO balls reveal a sharp decrease in weight at temperatures higher than 500 °C, owing to the combustion of the rGO sheets. The rGO sheets typically have low combustion temperatures around 350 °C. However, in this case, the rGO sheets, which constitute 17 and 15 wt % of the sandwich- and filled-structured GeO_x-coated rGO balls, respectively, have high combustion temperatures of 500 and 810 °C. In addition, the sandwich structure resulted in two-step combustion of rGO by protecting the contact of rGO with oxygen. The BET surface areas of the amorphous GeO_x-coated rGO composite powders with sandwich and filled structures were 35 and 6 m^2 g^{-1}, respectively. The GeO_x-coated rGO composite powders with sandwich structure had more well-developed mesopores than those of the powders with filled structure, as shown in Figure S5 in the SI.

The Li-ion storage properties of the GeO_x-coated rGO balls with sandwich and filled structures and the commercial GeO_2 powders were investigated via CV and galvanostatic charge/discharge measurements. Figure 4a shows the CV curves of the sandwich-structured GeO_x-coated rGO balls. These curves were obtained at a scan rate of 0.1 mV s^{-1} for potentials ranging from 0.001 to 1.2 V. In the first cathodic sweep, the peak at 0.9 V is attributed to the interfacial Li storage and formation of the solid electrolyte interface (SEI) layer on the surface of the GeO_x-coated rGO balls.[21−30] The broad peaks observed at voltages of 0.4 and 0.1 V are attributed to the conversion of GeO_x to Ge metal and amorphous Li_2O and the alloying of Ge and Li metals, respectively.[21−30] In the first anodic sweep, dealloying of the Li−Ge alloys occurs at ∼0.5 V.[21−30] From the second cycle onward, the cathodic and anodic curves in the CV scans overlap substantially, indicating that the electrodes of the GeO_x-coated rGO balls exhibit outstanding cyclability for repeated Li-ion insertion/extraction.

Figure 4b shows the first charge and discharge curves of the GeO_x-coated rGO balls with sandwich and filled structures and the commercial GeO_2 powders at a current density of 2 A g^{-1}. The first discharge curves of the GeO_x-coated rGO balls with sandwich and filled structures exhibit smooth long slopes between 1.0 and 0.001 V. On the other hand, the highly crystalline commercial GeO_2 powders exhibit a long plateau at a potential of 0.3 V. Similar phenomena have been reported for coarse-grained metal oxides, which are used as anode materials.[3] The GeO_x-coated rGO balls with sandwich and filled structures and the commercial GeO_2 powders had initial discharge capacities of 1908, 1758, and 2144 mA h g^{-1} and corresponding initial charge capacities of 795, 651, and 634 mA h g^{-1}, respectively. The high initial irreversible capacity losses result from the formation of SEI layers on the surface of the active materials and the formation of amorphous Li_2O materials.[21−28] Figure 4c shows the cycling performances of the three types of samples at a constant current density of 2 A g^{-1}. The initial discharge and charge capacities are not shown in Figure 4c. The GeO_x-coated rGO balls with sandwich and filled structures and the commercial GeO_2 powders delivered 700th-cycle charge capacities of 758, 579, and 361 mA h g^{-1} and corresponding capacity retentions of 95, 87, and 51%, respectively, as measured from the second cycle. The bare rGO microspheres prepared by spray pyrolysis delivered a reversible discharge capacity of 125 mA h g^{-1} at a current density of 2 A g^{-1}, as shown in Figure S6 in the SI. Therefore, the rGO contributed slightly to the capacities of the GeO_x-coated rGO balls with sandwich structure. The poor cycling performances of the commercial GeO_2 powders during repeated Li insertion and desertion processes result from their poor structural stability. This result indicates that the rGO sheets reduced the stress induced by volume expansion of the GeO_x materials, thereby resulting in improved cycle stability of the GeO_x-coated rGO balls. The TEM and elemental mapping images for the fully charged state after the 700th cycle (Figure S7 in the SI) reveal that the sandwich-structured GeO_x-coated rGO balls prevented the aggregation of GeO_x during cycling, thereby enhancing the cycle stability; the overall porous morphology of the balls was also maintained after cycling. The GeO_x-coated rGO balls with sandwich and filled structures were cycled at current densities ranging from 1 to 9 A g^{-1} (Figure 4d) in order to determine their rate performances. The charge and discharge curves for rate performance tests are shown in Figure S8 in the SI. At respective current densities of 1, 3, 5, 7, and 9 A g^{-1}, the former exhibits reversible charge capacities of 864, 728, 615, 525, and 450 mA h g^{-1} and the latter corresponding values of 789, 592, 426, 331, and 258 mA h g^{-1}. The rGO balls with sandwich and filled structures delivered reversible charge capacities of 858 and 793 mA h g^{-1}, respectively, when the current density was returned to 1 A g^{-1}. Furthermore, the porous balls with sandwich structure had faster Li-ion storage properties than their filled-structure counterparts. EIS analysis was performed in order to understand the superior rate performance of the balls with sandwich structure compared to that of the balls with filled structure. The semicircle in the high-to-medium-frequency region represents the charge-transfer resistance (R_{ct}) of the electrode.[55−58] In the low-frequency region, the straight line of the relationship between Z_{re} and $\omega^{-1/2}$ (where ω is the angular frequency in the low-frequency region, $\omega = 2\pi f$) helps in understanding the Li-ion diffusion properties. The small slope gradient of the straight line is indicative of good Li-ion kinetics in the electrode materials. The Nyquist plots of the GeO_x-coated rGO balls with sandwich and filled structures before cycling (Figure 5a) show that the semicircle of the former has a substantially smaller diameter than that of the latter. Accordingly, the charge-transfer resistance values of the balls with sandwich and filled structures are 39 and 103 Ω, respectively. In addition, in the low-frequency region (Figure 5b), the sandwich-structured balls exhibit lower slope than their filled-structure counterparts.[57,58] This lower slope is attributed to the macroporous rGO structure that facilitates electrolyte penetration into the powder, thereby resulting in a short Li-ion diffusion pathway. The long-term cycling performance of the GeO_x-coated rGO balls with sandwich structure at a high current density of 5 A g^{-1} is shown in Figure 6. The balls have 1st and 100th reversible charge capacities of 588 and 692 mA h g^{-1}, respectively. The reversible capacity increases from cycles 1 to 100 owing to the gradual conversion of GeO_x at the aforementioned high current density. Moreover, the balls exhibited a 1600th reversible charge capacity of 629 mA h g^{-1} and a corresponding capacity retention of 90.7%, as measured from the maximum reversible capacity at the 100th cycle. The porous GeO_x-coated rGO balls with sandwich structure exhibited excellent Li-ion storage

DOI: 10.1021/acsami.5b02846
ACS Appl. Mater. Interfaces 2015, 7, 13952−13959

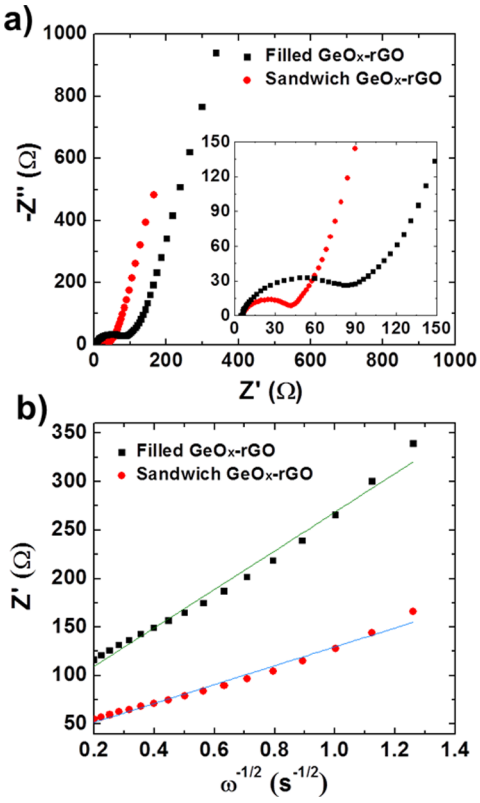

Figure 5. EIS and relationship between Z' and $\omega^{-1/2}$ in the low-frequency region of the amorphous GeO_x-coated rGO balls with sandwich and filled structures. (a) Nyquist plots before cycling and (b) linear fits in the low-frequency region before cycling.

properties owing to the synergistic effect of the amorphous GeO_x materials and the porous rGO ball structure.

4. CONCLUSIONS

In this study, the electrochemical properties of amorphous GeO_x-coated rGO composite powders with sandwich and filled structures, which were prepared by one-pot spray pyrolysis, were compared to those of commercially produced GeO_2 powders. The large amount of uniformly coated amorphous GeO_x in the rGO ball resulted in superior Li-ion storage properties of the GeO_x/rGO composite powders compared to those of the commercial GeO_2 powders. The nanovoids formed by decomposition of the PS nanobeads improved the Li-ion storage properties of the GeO_x/rGO composite powders at high current densities by shortening the Li-ion diffusion pathway. In addition, the amorphous GeO_x-coated rGO composite powders, which have an ideal structure for the anode materials of high-performance Li-ion batteries, exhibited high stable reversible capacities and exceptional long-term cycling performance.

■ ASSOCIATED CONTENT

Supporting Information

Schematic diagram of the spray-pyrolysis process, XRD pattern of the commercial GeO_2 powders, XPS spectra of the amorphous GeO_x-coated rGO balls with filled structure, Raman spectrum of the sandwich-structured GeO_x/rGO balls, pore distributions of the amorphous GeO_x-coated rGO balls with sandwich and filled structures, cycling performance of the bare rGO microspheres, TEM and elemental mapping images of the amorphous GeO_x-coated rGO balls with sandwich structure after the 700th cycle, charge/discharge curves of the amorphous GeO_x-coated rGO composite powders with sandwich and filled structures at a various current densities, and FE-SEM images of the commercial GeO_2 powders. The Supporting Information is available free of charge on the ACS Publications website at DOI: 10.1021/acsami.5b02846.

■ AUTHOR INFORMATION

Corresponding Author

*E-mail: yckang@korea.ac.kr. Tel.: +82-2-928-3584. Fax: +82-2-3290-3268.

Notes

The authors declare no competing financial interest.

■ ACKNOWLEDGMENTS

This work was supported by the Energy Efficiency & Resources Core Technology Program of the Korea Institute of Energy Technology Evaluation and Planning and granted financial resources from the Ministry of Trade, Industry & Energy, Republic of Korea (Grant 201320200000420).

■ REFERENCES

(1) Aricò, A. S.; Bruce, P.; Scrosati, B.; Tarascon, J.-M.; Schalkwijk, W. Nanostructured Materials for Advanced Energy Conversion and Storage Devices. *Nat. Mater.* **2005**, *4*, 366−377.

(2) McDowell, M. T.; Lee, S. W.; Nix, W. D.; Cui, Y. 25th Anniversary Article: Understanding the Lithiation of Silicon and Other Alloying Anodes for Lithium-Ion Batteries. *Adv. Mater.* **2013**, *25*, 4966−4985.

(3) Reddy, M. V.; Rao, G. V. S.; Chowdari, B. V. R. Metal Oxides and Oxysalts as Anode Materials for Li Ion Batteries. *Chem. Rev.* **2013**, *113*, 5364−5457.

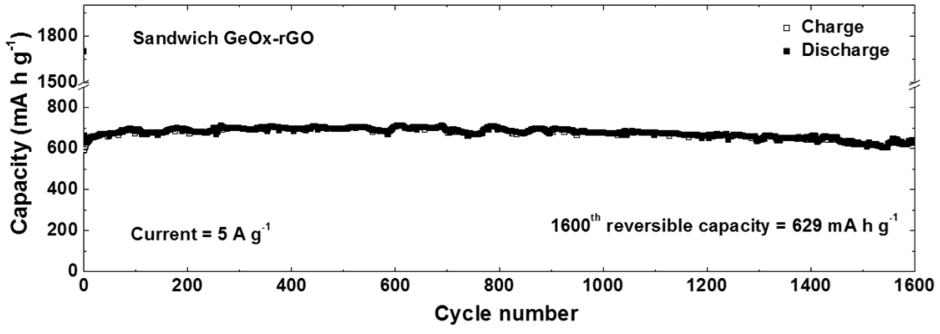

Figure 6. Long-term cycling performance of the amorphous GeO_x-coated rGO composite powders with sandwich structure at a current density of 5 A g^{-1}.

DOI: 10.1021/acsami.5b02846
ACS Appl. Mater. Interfaces 2015, 7, 13952−13959

(4) Uchakera, E.; Cao, G. Mesocrystals as Electrode Materials for Lithium-Ion Batteries. *Nano Today* **2014**, *9*, 499−524.
(5) Su, X.; Wu, Q.; Li, J.; Xiao, X.; Lott, A.; Lu, W.; Sheldon, B. W.; Wu, J. Silicon-Based Nanomaterials for Lithium-Ion Batteries: A Review. *Adv. Energy Mater.* **2014**, *4*, 1300882.
(6) Choi, N.-S.; Chen, Z.; Freunberger, S. A.; Ji, X.; Sun, Y.-K.; Amine, K.; Yushin, G.; Nazar, L. F.; Cho, J.; Bruce, P. G. Challenges Facing Lithium Batteries and Electrical Double-Layer Capacitors. *Angew. Chem., Int. Ed.* **2012**, *51*, 9994−10024.
(7) Chen, J. S.; Lou, X. W. SnO_2-Based Nanomaterials: Synthesis and Application in Lithium-Ion Batteries. *Small* **2013**, *9*, 1877−1893.
(8) Lin, N.; Zhou, J.; Wang, L.; Zhu, Y.; Qian, Y. Polyaniline-Assisted Synthesis of Si@C/RGO as Anode Material for Rechargeable Lithium-Ion Batteries. *ACS Appl. Mater. Interfaces* **2015**, *7*, 409−414.
(9) Li, X.; Gu, M.; Hu, S.; Kennard, R.; Yan, P.; Chen, X.; Wang, C.; Sailor, M. J.; Zhang, J.-G.; Liu, J. Mesoporous Silicon Sponge as an Anti-Pulverization Structure for High-Performance Lithium-Ion Battery Anodes. *Nat. Commun.* **2014**, *5*, 4105.
(10) Kwon, T. W.; Jeong, Y. K.; Lee, I.; Kim, T.-S.; Choi, J. W.; Coskun, A. *Adv. Mater.* **2014**, *26*, 7979−7985.
(11) Zhang, W.-M.; Hu, J.-S.; Guo, Y.-G.; Zheng, S.-F.; Zhong, L.-S.; Song, W.-G.; Wan, L.-J. Tin-Nanoparticles Encapsulated in Elastic Hollow Carbon Spheres for High-Performance Anode Material in Lithium-Ion Batteries. *Adv. Mater.* **2008**, *20*, 1160−1165.
(12) Zhu, Z.; Wang, S.; Du, J.; Jin, Q.; Zhang, T.; Cheng, F.; Chen, J. Ultrasmall Sn Nanoparticles Embedded in Nitrogen-Doped Porous Carbon as High-Performance Anode for Lithium-Ion Batteries. *Nano Lett.* **2014**, *14*, 153−157.
(13) Chen, X.; Li, X.; Ding, F.; Xu, W.; Xiao, J.; Cao, Y.; Meduri, P.; Liu, J.; Graff, G. L.; Zhang, J.-G. Conductive Rigid Skeleton Supported Silicon as High-Performance Li-Ion Battery Anodes. *Nano Lett.* **2012**, *12*, 4124−4130.
(14) Seng, K. H.; Park, M.-H.; Guo, Z. P.; Liu, H. K.; Cho, J. Self-Assembled Germanium/Carbon Nanostructures as High-Power Anode Material for the Lithium-Ion Battery. *Angew. Chem., Int. Ed.* **2012**, *51*, 5657−5661.
(15) Chan, C. K.; Zhang, X. F.; Cui, Y. High Capacity Li Ion Battery Anodes Using Ge Nanowires. *Nano Lett.* **2008**, *8*, 307−309.
(16) Jin, S.; Li, N.; Cui, H.; Wang, C. Embedded into Graphene Ge Nanoparticles Highly Dispersed on Vertically Aligned Graphene with Excellent Electrochemical Performance for Lithium Storage. *ACS Appl. Mater. Interfaces* **2014**, *6*, 19397−19404.
(17) Yuan, F.-W.; Yang, H.-J.; Tuan, H.-Y. Alkanethiol-Passivated Ge Nanowires as High-Performance Anode Materials for Lithium-Ion Batteries: The Role of Chemical Surface Functionalization. *ACS Nano* **2012**, *6*, 9932−9942.
(18) Ngo, D. T.; Kalubarme, R. S.; Le, H. T. T.; Fisher, J. G.; Park, C.-N.; Kim, I.-D.; Park, C.-J. Carbon-Interconnected Ge Nanocrystals as an Anode with Ultra-Long-Term Cyclability for Lithium Ion Batteries. *Adv. Funct. Mater.* **2014**, *24*, 5291−5298.
(19) Xue, D.-J.; Xin, S.; Yan, Y.; Jiang, K.-C.; Yin, Y.-X.; Guo, Y.-G.; Wan, L.-J. Improving the Electrode Performance of Ge through Ge@C Core−Shell Nanoparticles and Graphene Networks. *J. Am. Chem. Soc.* **2012**, *134*, 2512−2515.
(20) Seng, K. H.; Park, M.-H.; Guo, Z. P.; Liu, H. K.; Cho, J. Catalytic Role of Ge in Highly Reversible GeO_2/Ge/C Nanocomposite Anode Material for Lithium Batteries. *Nano Lett.* **2013**, *13*, 1230−1236.
(21) Jin, S.; Li, N.; Cui, H.; Wang, C. Growth of the Vertically Aligned Graphene@Amorphous GeO_x Sandwich Nanoflakes and Excellent Li Storage Properties. *Nano Energy* **2013**, *2*, 1128−1136.
(22) Lv, D.; Gordin, M. L.; Yi, R.; Xu, T.; Song, J.; Jiang, Y.-B.; Choi, D.; Wang, D. GeO_x/Reduced Graphene Oxide Composite as an Anode for Li-Ion Batteries: Enhanced Capacity via Reversible Utilization of Li_2O along with Improved Rate Performance. *Adv. Funct. Mater.* **2014**, *24*, 1059−1066.
(23) Wang, X.-L.; Han, W.-Q.; Chen, H.; Bai, J.; Tyson, T. A.; Yu, X.-Q.; Wang, X.-J.; Yang, X.-Q. Amorphous Hierarchical Porous GeO_x as High-Capacity Anodes for Li Ion Batteries with Very Long Cycling Life. *J. Am. Chem. Soc.* **2011**, *133*, 20692−20695.
(24) Li, X.; Liang, J.; Hou, Z.; Zhu, Y.; Wang, Y.; Qian, Y. Coordination Complex Pyrolyzation for the Synthesis of Nanostructured GeO_2 with High Lithium Storage Properties. *Chem. Commun.* **2014**, *50*, 13956−13959.
(25) Jahel, A.; Darwiche, A.; Ghimbeu, C. M.; Vix-Guterl, C.; Monconduit, L. High Cycleability Nano-GeO_2/Mesoporous Carbon Composite as Enhanced Energy Storage Anode Material in Li-Ion Batteries. *J. Power Sources* **2014**, *269*, 755−759.
(26) Jia, F.; Song, L.; Wei, W.; Qu, P.; Xu, M. Facile One-Pot Method Synthesis CNT−GeO_2 Nanocomposite for High Performance Li Ion Battery Anode Material. *New J. Chem.* **2015**, *39*, 689−695.
(27) Son, Y.; Park, M.; Son, Y.; Lee, J.-S.; Jang, J.-H.; Kim, Y.; Cho, J. Quantum Confinement and Its Related Effects on the Critical Size of GeO_2 Nanoparticles Anodes for Lithium Batteries. *Nano Lett.* **2014**, *14*, 1005−1010.
(28) Wei, W.; Guo, L. One-Step In Situ Synthesis of GeO_2/Graphene Composites Anode for High-Performance Li-Ion Batteries. *Part. Part. Syst. Charact.* **2013**, *30*, 658−661.
(29) Liu, B.; Abouimrane, A.; Balasubramanian, M.; Ren, Y.; Amine, K. GeO_2−SnCoC Composite Anode Material for Lithium-Ion Batteries. *J. Phys. Chem. C* **2014**, *118*, 3960−3967.
(30) Cho, Y. J.; Im, H. S.; Kim, H. S.; Myung, Y.; Back, S. H.; Lim, Y. R.; Jung, C. S.; Jang, D. M.; Park, J.; Cha, E. H.; Cho, W. I.; Shojaei, F.; Kang, H. S. Tetragonal Phase Germanium Nanocrystals in Lithium Ion Batteries. *ACS Nano* **2013**, *7*, 9075−9084.
(31) Lim, Y. R.; Im, H. S.; Cho, Y. J.; Park, J.; Cha, E. H.; Cho, W. I. Composition-Tuned $Sn_xGe_{1-x}S$ Nanocrystals for Enhanced-Performance Lithium Ion Batteries. *RSC Adv.* **2014**, *4*, 60058−60063.
(32) Cho, Y. J.; Im, H. S.; Myung, Y.; Kim, C. H.; Kim, H. S.; Back, S. H.; Lim, Y. R.; Jung, C. S.; Jang, D. M.; Park, J.; Cha, E. H.; Choo, S. H.; Song, M. S.; Cho, W. I. Germanium Sulfide(II and IV) Nanoparticles for Enhanced Performance of Lithium Ion Batteries. *Chem. Commun.* **2013**, *49*, 4661−4663.
(33) Luo, B.; Wang, B.; Li, X.; Jia, Y.; Liang, M.; Zhi, L. Graphene-Confined Sn Nanosheets with Enhanced Lithium Storage Capability. *Adv. Mater.* **2012**, *24*, 3538−3543.
(34) Liu, J. Charging Graphene for Energy. *Nat. Nanotechnol.* **2014**, *9*, 739−741.
(35) Li, Q.; Mahmood, N.; Zhu, J.; Hou, Y.; Sun, S. Graphene and its Composites with Nanoparticles for Electrochemical Energy Applications. *Nano Today* **2014**, *9*, 668−683.
(36) Huang, X.; Zeng, Z.; Fan, Z.; Liu, J.; Zhang, H. Graphene-Based Electrodes. *Adv. Mater.* **2012**, *24*, 5979−6004.
(37) Wu, Z.-S.; Zhou, G.; Yin, L.-C.; Ren, W.; Li, F.; Cheng, H.-M. Graphene/Metal Oxide Composite Electrode Materials for Energy Storage. *Nano Energy* **2012**, *1*, 107−131.
(38) Xin, S.; Guo, Y.-G.; Wan, L.-J. Nanocarbon Networks for Advanced Rechargeable Lithium Batteries. *Acc. Chem. Res.* **2012**, *45*, 1759−1769.
(39) Jiang, J.; Li, Y.; Liu, J.; Huang, X.; Yuan, C.; Lou, X. W. Recent Advances in Metal Oxide-based Electrode Architecture Design for Electrochemical Energy Storage. *Adv. Mater.* **2012**, *24*, 5166−5180.
(40) Zhou, M.; Cai, T.; Pu, F.; Chen, H.; Wang, Z.; Zhang, H.; Guan, S. Graphene/Carbon-Coated Si Nanoparticle Hybrids as High-Performance Anode Materials for Li-Ion Batteries. *ACS Appl. Mater. Interfaces* **2013**, *5*, 3449−3455.
(41) Hu, S.; Yin, F.; Uchaker, E.; Chen, W.; Zhang, M.; Zhou, J.; Qi, Y.; Cao, G. Facile and Green Preparation for the Formation of MoO_2−GO Composites as Anode Material for Lithium-Ion Batteries. *J. Phys. Chem. C* **2014**, *118*, 24890−24897.
(42) Chen, Z.; Ren, W.; Gao, L.; Liu, B.; Pei, S.; Cheng, H.-M. Three-Dimensional Flexible and Conductive Interconnected Graphene Networks Grown by Chemical Vapour Deposition. *Nat. Mater.* **2011**, *10*, 424−428.
(43) Luo, J.; Jang, H. D.; Sun, T.; Xiao, L.; He, Z.; Katsoulidis, A. P.; Kanatzidis, M. G.; Gibson, J. M.; Huang, J. Compression and

DOI: 10.1021/acsami.5b02846
ACS Appl. Mater. Interfaces 2015, 7, 13952−13959

Aggregation-Resistant Particles of Crumpled Soft Sheets. *ACS Nano* **2011**, *5*, 8943−8949.
(44) Yoon, S.-M.; Choi, W. M.; Baik, H.; Shin, H.-J.; Song, I.; Kwon, M.-S.; Bae, J. J.; Kim, H.; Lee, Y. H.; Choi, J.-Y. Synthesis of Multilayer Graphene Balls by Carbon Segregation from Nickel Nanoparticles. *ACS Nano* **2012**, *6*, 6803−6811.
(45) He, X.; Zhang, H.; Zhang, H.; Li, X.; Xiao, N.; Qiu, J. Direct Synthesis of 3D Hollow Porous Graphene Balls from Coal Tar Pitch for High Performance Supercapacitors. *J. Mater. Chem. A* **2014**, *2*, 19633−19640.
(46) Mao, S.; Wen, Z.; Kim, H.; Lu, G.; Hurley, P.; Chen, J. A General Approach to One-Pot Fabrication of Crumpled Graphene-Based Nanohybrids for Energy Applications. *ACS Nano* **2012**, *6*, 7505−7513.
(47) Choi, S. H.; Kang, Y. C. Crumpled Graphene−Molybdenum Oxide Composite Powders: Preparation and Application in Lithium-Ion Batteries. *ChemSusChem* **2014**, *7*, 523−528.
(48) Choi, B. G.; Yang, M. H.; Hong, W. H.; Choi, J. W.; Huh, Y. S. 3D Macroporous Graphene Frameworks for Supercapacitors with High Energy and Power Densities. *ACS Nano* **2012**, *6*, 4020−4028.
(49) Zhang, T. Y.; Li, X. Q.; Kang, S. Z.; Qin, L. X.; Yan, W. F.; Mua, J. Facile Assembly and Properties of Polystyrene Microsphere/Reduced Graphene Oxide/Ag Composite. *J. Colloid Interface Sci.* **2013**, *402*, 279−283.
(50) Negishi, Y.; Nagao, S.; Nakamura, Y.; Nakajima, A. Visible Photoluminescence of the Deposited Germanium−Oxide Prepared from Clusters in the Gas Phase. *J. Appl. Phys.* **2000**, *88*, 6037.
(51) Beidaghi, M.; Wang, C. Micro-Supercapacitors Based on Interdigital Electrodes of Reduced Graphene Oxide and Carbon Nanotube Composites with Ultrahigh Power Handling Performance. *Adv. Funct. Mater.* **2012**, *22*, 4501−4510.
(52) Choi, S. H.; Jung, D. S.; Choi, J. W.; Kang, Y. C. Superior Lithium-Ion Storage Properties of Si-Based Composite Powders with Unique Si@Carbon@Void@Graphene Configuration. *Chem.—Eur. J.* **2015**, *21*, 2076−2082.
(53) Liu, C. L.; Dong, W. S.; Song, J. R.; Liu, L. Evolution of Microstructure and Properties of Phenolic Fibers during Carbonization. *Mater. Sci. Eng., A* **2007**, *459*, 347−354.
(54) Stankovich, S.; Dikin, D. A.; Piner, R. D.; Kohlhaas, K. A.; Kleinhammes, A.; Jia, Y.; Wu, Y.; Nguyen, S. T.; Ruoff, R. S. Synthesis of Graphene-Based Nanosheets via Chemical Reduction of Exfoliated Graphite Oxide. *Carbon* **2007**, *45*, 1558−1565.
(55) Reddy, M. V.; Yu, T.; Sow, C.-H.; Shen, Z. X.; Lim, C. T.; Rao, G. V. S.; Chowdari, B. V. R. α-Fe_2O_3 Nanoflakes as an Anode Material for Li-Ion Batteries. *Adv. Funct. Mater.* **2007**, *17*, 2792−2799.
(56) Guo, J.; Sun, A.; Chen, X.; Wang, C.; Manivannan, A. Cyclability Study of Silicon−Carbon Composite Anodes for Lithium-Ion Batteries Using Electrochemical Impedance Spectroscopy. *Electrochim. Acta* **2011**, *56*, 3981−3987.
(57) Ko, Y. N.; Park, S. B.; Jung, K. Y.; Kang, Y. C. One-Pot Facile Synthesis of Ant-Cave-Structured Metal Oxide−Carbon Microballs by Continuous Process for Use as Anode Materials in Li-Ion Batteries. *Nano Lett.* **2013**, *13*, 5462−5466.
(58) Du, X.; He, W.; Zhang, X.; Yue, Y.; Liu, H.; Zhang, X.; Min, D.; Ge, X.; Du, Y. Enhancing the Electrochemical Performance of Lithium Ion Batteries Using Mesoporous $Li_3V_2(PO_4)_3$/C Microspheres. *J. Mater. Chem.* **2012**, *22*, 5960−5969.

DOI: 10.1021/acsami.5b02846
ACS Appl. Mater. Interfaces 2015, 7, 13952−13959